The sky is made of lava: how lava worlds reveal their interiors through their atmospheres

Buchem, C.P.A. van

3 Sensitivity of Dry Lava Planet Atmospheric Emission Spectra to Changes in Lava Compositions

Work in review **C. P. A. van Buchem**, R. Buddhacharya, M. Zilinskas, S. Zieba, Y. Miguel, W. van Westrenen, *Monthly Notices of the Royal Astronomical Society.* Reprinted here in its entirety.

Abstract

The atmospheres of hot rocky exoplanets are among the first primary targets of the JWST. Interpreting their atmospheric spectra requires understanding the link between silicate lava compositions and overlying atmospheres. We investigate the sensitivity of simulated emission spectra of dry lava planets to variations in oxide abundances in silicate melt. Our goal is to determine which molten surface features could be distinguishable with future observations. We combine our vaporisation code with gas chemical equilibrium and radiative transfer codes to self-consistently compute atmospheric chemistry and thermal structure. Alongside varying lava compositions, we assess the impact of host star spectral type on emission spectra. TiO_2 melt abundance dictates atmospheric TiO, which strongly influences surface temperature and emission spectra due to its short-wave opacity. This creates a degeneracy with heat redistribution efficiency, potentially broken by observing the optical TiO emission feature. Atmospheric SiO and SiO_2 abundances depend on melt SiO_2 content, with stronger SiO and SiO_2 emission features at higher melt abundances. For TiO_2 and SiO_2, these effects are at JWST's detection limit with six eclipses. Variations in alkali abundances could cause large surface pressure changes and influence the abundance of atmospheric SiO and SiO_2. Overall, melt composition has a limited impact on emission spectra, but some observable changes exist. TiO_2 and SiO_2 are the most influential species, with alkalis playing a minor role.

3.1 Introduction

Hot rocky exoplanets (HREs) serve as potential windows into rocky planet compositions and interiors. Their highly irradiated molten surfaces partially vaporise, significantly influencing the thickness and composition of the overlying atmosphere, providing a direct connection between their interior and their atmosphere (Léger et al. 2009; Henning et al. 2018; Boukaré et al. 2022). The composition of the atmosphere should therefore be strongly linked to the composition of the surface melt, an idea that has been the premise of a quickly growing body of theoretical and modelling work over the past years (e.g. Schaefer & Fegley Jr. 2004; Miguel et al. 2011; Ito et al. 2015; Kite et al. 2016; Nguyen et al. 2020; Zilinskas et al. 2022; Wolf et al. 2023; van Buchem et al. 2023; Seidler et al. 2024).

JWST has brought us from theory and modelling into an era where we can start inferring atmospheric compositions of rocky planets (Zieba et al. 2023; Hu et al. 2024). With many new observations on the way and the prospect on the horizon of additional measurements by the ELT and Ariel, it is key to understand how the compositions of lava oceans influence the atmospheric properties of HREs and the impact this has on the emission spectra we may observe.

To date, most previous work has assumed that the composition of day-side lava oceans is either equal to that of the bulk silicate Earth (BSE) (Palme & O'Neill 2003), or to a range of silicate melt compositions typically erupted on the surface of the Earth (e.g. Hans Wedepohl 1995; Schaefer & Fegley 2009; Miguel et al. 2011; Gale et al. 2013). Although this is certainly justifiable as a starting point, it is becoming increasingly clear that the compositional variability of rocky planetary crusts and mantles can be significantly larger than the range covered by these initial assumptions. Estimating the bulk composition of rocky exoplanets (Guimond et al. 2024) is an active area of research with estimates being made based on their measured density (Rogers & Seager 2010; Swift et al. 2011; Dorn et al. 2015), the compositions of their host-stars (Carter-Bond et al. 2012; Santos et al. 2017; Putirka & Rarick 2019; Putirka et al. 2021; Wang et al. 2022) and by analysing polluted white dwarfs (Klein et al. 2011; Bonsor et al. 2021; Putirka & Xu 2021; Xu & Bonsor 2021).

In addition, the bulk composition of a rocky exoplanet can only be assumed to be equal to the composition of surface lava if no interior differentiation has taken place - which is unlikely based on observations from our own solar system. Metallic core formation significantly depletes the silicate reservoirs of rocky bodies in iron and siderophile (iron-loving) elements (e.g. Hinkel & Unterborn 2018; Seidler et al. 2024). Subsequent crust-mantle differentiation can lead to surface compositions that differ substantially from mantle compositions (e.g. Lin et al. 2017; Hakim et al. 2019b,a). Temporal changes in melt composition can also take place due to chemical evolution of the melt as a result of the depletion of volatile melt species (Schaefer & Fegley Jr. 2004; Kite et al. 2016)

or due to crystal formation during lava cooling (Iezzi et al. 2008; Lichtenberg et al. 2021; Payacán et al. 2023).

Due to the large number of uncertainties and degeneracies surrounding the potential compositions of a surface melt, we investigate how deviations from the canonical BSE composition (Palme & O'Neill 2003) affect the atmospheres and spectral properties of HREs. In this work, we assume the HREs to be 'dry', by which we mean that we do not include any volatile species. Although recent work is pointing towards the possibility of HREs supporting volatile-rich atmospheres (Zilinskas et al. 2023; Piette et al. 2023; Hu et al. 2024), we limit the scope of this study to investigating the effect of varying individual oxide abundances in dry circumstances. This serves as a basis to compare with observations from JWST and other future efforts such as ELT and Ariel, and to identify, where possible, potential fingerprints in atmospheric emission spectra of specific compositional features of the lava underlying these atmospheres.

In the following section, we give a description of how we combined different thermochemical and radiative codes to produce self-consistent pseudo-2D emission spectra for a range of different star-planet system parameters and varying melt compositions. In section 3.3, we show the most relevant results out of the wide range of models that we ran, highlighting the potentially distinguishing features in the emission spectra. In section 3.4, we discuss the caveats and nuances that need to be taken into account when interpreting these results. Finally, we present our conclusions in section 3.5.

3.2 Method

The aim of this paper is to produce emission spectra for volatile-free HREs with a range of different surface melt compositions. In order to achieve this, we took an approach similar to that of Zilinskas et al. (2022):

1. **Determine the melt composition:** Using BSE (Palme & O'Neill 2003) as a starting point, we vary the abundance of each of the oxides in the melt, keeping the relevant abundances of all other melt components the same.

2. **Calculate the composition of the melt vapour:** The melt composition and an initial guess of the equilibrium temperature at the chosen point on the planet surface are given as input to our melt-atmosphere chemical equilibrium code LavAtmos (van Buchem et al. 2023). LavAtmos calculates the equilibrium chemical composition of the vapour coming from the melt. This is then converted to elemental abundances and passed on to the next step.

3. **Calculate the equilibrium gas chemistry over a grid of temperature-pressure (TP) values:** With the elemental abundances calculated in the previous step and a wide TP grid as input, we use the gas-phase chemical equilibrium code FastChem 3 (**?**) to calculate the gas chemistry over the entire grid.

4. **Iteratively determine a TP profile:** Star-planet system parameters and the gas-chemistry over the TP grid from the previous step are given as input to the radiative transfer code `HELIOS` 3 (Malik et al. 2017). `HELIOS` produces an atmospheric temperature-pressure profile.

   We then compare the surface temperature found by `HELIOS` with the initial surface temperature assumed for the melt-vapour calculation done in step **1**. If these values are not consistent with each other, we repeat step **1** using the newly calculated surface temperature as input. This loop is repeated until the surface temperature converges.

5. **Calculate the equilibrium gas chemistry over the final converged TP profile:** FastChem is used once more to calculate the equilibrium gas-chemistry along the final TP profile.

6. **Produce the emission spectrum:** We pass on the output of the chemistry and temperature structure to another radiative transfer code petitRADTRANS (Mollière et al. 2019), which we use to compute the final emission spectrum.

Following these steps allowed us to produce self-consistent 1D models of HRE atmospheres. In the remainder of this section, we explain how we varied the melt composition, the equilibrium chemistry of LavAtmos and FastChem, the radiative transfer codes `HELIOS` and petitRADTRANS, the pseudo-2D model that we used to produce the final spectra, and finally the different star-planet systems we tested.

3.2.1 Melt compositions

As explained in section 3.1, significant uncertainty remains about the extent to which lava compositions on the day-side of HREs can differ from a canonical BSE model. Hence, our aim is not to define likely compositions of the lava oceans of HREs but instead to investigate how deviating from the canonical BSE major element composition (Palme & O'Neill 2003) affects atmospheric composition, thermal structure, and emission spectra.

For each of the eight oxide components included in the canonical melt composition (SiO_2, MgO, Al_2O_3, TiO_2, FeO, CaO, Na_2O, and K_2O) we varied

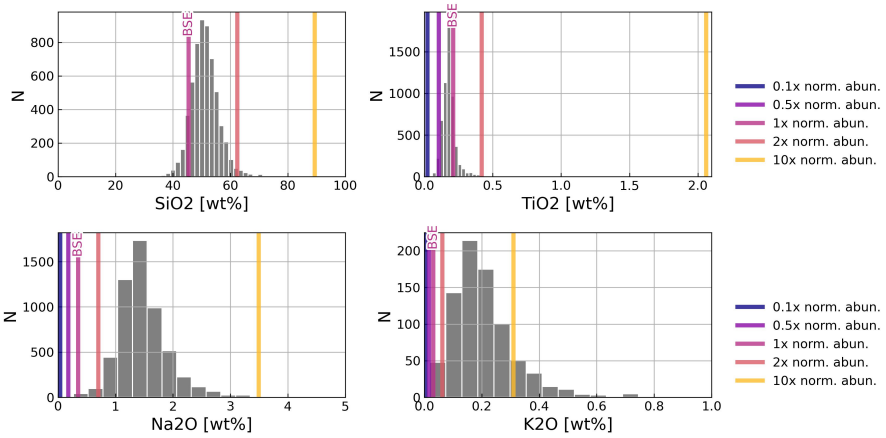

Figure 3.1: Abundance distributions derived from stellar compositions: Based on the work by Putirka & Rarick (2019), we plot the weight percentage distributions of the 4 most impactful melt oxides according to this work. These weight percentages were determined for hypothetical compositions based on the stellar compositions available in the Hypatia catalogue (Hinkel & Burger 2017). The vertical plotted lines represent the abundance ranges in weight percentage that we tested for each oxide, as detailed in the main text.

their original BSE abundance individually by factors 0.1, 0.5, 2, and 10 - spanning two orders of magnitude. The only exception was SiO_2, which was only modelled for x2 and x10 the BSE abundance due to MELTS (the underlying thermodynamics code used by LavAtmos - see section 3.2.2) not being able to run for compositions with low SiO_2 abundance.

Within the vaporisation code, given species abundances are normalized to 100 per cent. For example, when increasing the amount of SiO_2 in BSE by a factor of 10 from 45.4% to 454%, with all other percentages remaining equal to BSE values, the actual bulk composition that is used in the vaporization is renormalized to 89% (with a corresponding decrease of the other oxide species). These final normalised values are reflected in the values plotted in Figure 3.1. In Table 3.2, we provide an overview of the different weight percentages used for the melt oxide species that we tested as well as their normalized counterparts.

In Figure 3.1, we plotted the tested weight percentages for SiO_2, TiO_2, Na_2O, and K_2O alongside the distribution of 'bulk silicate planet'[1] compositions derived by Putirka & Rarick (2019) based on stellar compositions recorded in the Hypatia catalogue (Hinkel & Burger 2017). We selected these oxides due to them being the most impactful on the emission spectrum of HREs (see section 3.3). Figure 3.1 also shows that the tested oxide variations encompass all but a few of the expected edge cases for SiO_2 and K_2O. The biggest outlier is

[1] Bulk composition of a planet that excludes an iron-rich metallic core.

TiO_2, where the 10x abundance is 2.06% while the maximum value calculated by Putirka & Rarick (2019) is around 0.42%. Even so, we consider these abundances to be a conservative estimate of the extremes that could be reached in crust-mantle differentiation and in chemically evolved lava oceans, which we discuss in detail in section 3.4.1.

3.2.2 Equilibrium chemistry

In order to calculate the composition of the vapour above a melt for a given temperature (step **1**), we use our thermochemical equilibrium code LavAtmos (van Buchem et al. 2023)[2]. The partial pressure of any vapour above a melt can be calculated by solving the following equation:

$$P_{ij} = K_{r_{ij}}(T, P) a_j^{c_{ij}} P_{\mathrm{O_2}}^{d_{ij}} \tag{3.1}$$

Where P_{ij} is the partial pressure of vapour species i as formed in the vaporization of melt end-member species j, $K_{r_{ij}}$ is the temperature and pressure dependent chemical equilibrium constant of the corresponding vaporization reaction r, a_j is the activity of the melt end-member species, $P_{\mathrm{O_2}}$ is the O_2 partial pressure, and c_{ij} and d_{ij} are the stoichiometric coefficients necessary to balance the reaction. LavAtmos derives $K_{r_{ij}}$ for each reaction included from the thermodynamic data found in the JANAF database (Chase 1998). The activity a_j of each end-member species in the melt is calculated by using the geochemical code `MELTS` (Ghiorso & Sack 1995; Asimow & Ghiorso 1998; Ghiorso et al. 2002; Gualda et al. 2012; Ghiorso & Gualda 2015) through the ThermoEngine python wrapper[3]. Finally, LavAtmos solves for the O_2 partial pressure ($P_{\mathrm{O_2}}$) using the laws of mass action and mass balance as constraints. The included oxides are SiO_2, MgO, Al_2O_3, TiO_2, FeO, CaO, Na_2O, and K_2O.

Zilinskas et al. (2022) relied on published outputs of the `MAGMA` (Fegley & Cameron 1987; Schaefer & Fegley Jr. 2004) code to determine the vapour compositions above a melt. A key difference in the approach taken in this paper is the fact that using LavAtmos allows for far greater flexibility in testing different surface melt compositions. LavAtmos and `MAGMA` differ from each other mainly in the way in which the activities of the end-member oxide species in the melt are calculated. Instead of `MELTS`, `MAGMA` makes use of the Ideal Mixing of Complex Components (IMCC) model (Hastie et al. 1982b; Hastie & Bonnell 1985, 1986). This leads to some differences in calculated partial pressure (mainly for K); however, they generally agree well with each other, as shown in van Buchem et al. (2023).

Another recently published open-source vaporization code is VapoRock (Wolf et al. 2023). This works very similarly to LavAtmos by using `MELTS`

[2] A recently published update of the code (van Buchem et al. 2024) allows for the inclusion of volatile elements, but we focus the work in this paper on volatile-free atmospheres.

[3] https://gitlab.com/ENKI-portal/ThermoEngine

to calculate the activities of liquid oxide species in the melt and solving equation 3.1 for each included vaporization reaction. However, it treats P_{O_2} as a free parameter given as input by the user instead of constraining it using the laws of mass action and mass balance. A similar approach to this is also taken in the work by Seidler et al. (2024), who use an altered version of the `MAGMA` code that allows the fO_2 to be treated as a free parameter. The drawbacks of not constraining P_{O_2} using mass action and mass balance are twofold. First, imposing a P_{O_2} value other than that which satisfies mass action and mass balance, means that oxygen is being added or removed from the system - depending on if its partial-pressure is higher or lower than the value that satisfies these constraints. Second, it does not allow for P_{O_2} to change self-consistently as the composition of the melt evolves. With LavAtmos, we can consistently account for these changes when testing different compositions.

In Seidler et al. (2024) it is argued that the approach taken to calculate P_{O_2} in `MAGMA` and LavAtmos is only valid if all possible vaporisation reactions that could release O_2 are taken into account and if the set of melt components and their thermodynamic properties is complete and accurate. For the nine included end-member components of the melt, LavAtmos includes 30 of the most important vaporisation reactions, of which 26 involve O_2 (van Buchem et al. 2023). At 4000 K for a BSE melt composition, the partial pressure of the least abundant vapour species (Al_2) is just above 1e-9 bar, while the partial pressure of O_2 is just under 1 bar. At colder temperatures, the difference between these partial pressures grows further. Including the vaporisation reactions of the less abundant vapour species would likely not significantly alter the calculated O_2 partial pressure. Similarly, including a greater number of refractory oxide species in the thermodynamic melt model would likely only have a marginal impact on the O_2 partial pressure. Concerning the accuracy of the thermodynamic properties, we agree that this is something that should be looked into - however, since both Vaporock and `MAGMA` also make extensive use of the JANAF tables, this issue is not unique to LavAtmos. Hence, in our view, LavAtmos provides an approximation of the vapour composition that is accurate enough for the work presented in this paper.

In order to isolate the effect of changing oxide abundances on the atmospheres and resulting emission spectra of HREs, we do not consider the effect that the presence of volatiles in a melt may have on vaporisation. We assume that no volatile elements (eg. H, C, N, S, and P) are present in either the atmosphere or the melt.

As explained prior, the chemical composition of the melt vapor is converted to elemental abundances and passed on to the gas chemical equilibrium code FastChem 3 (Stock et al. 2018, 2022; Kitzmann et al. 2024), which is used to calculate the gas-chemistry of the atmosphere. Initially, this is done over a temperature-pressure grid (step **2**) and then again over the final TP profile (step **4**). The majority of the thermal data used by FastChem 3 for this work is from Chase (1998), see the appendix of Kitzmann et al. (2024) for a full

Table 3.1: Overview of tested star-planet systems: For each spectral type, generic stellar values were used. The orbital distance of each of the planets was determined such that the substellar equilibrium temperature is 3000 K. The planets all have the same assumed radius of 1.5 R_{earth}.

Spectral type	M_{star} [$M_\odot$]	R_{star} [$R_\odot$]	T_{star} [K]	Orbital distance [AU]
F	1.3	1.23	6000	2.29e-2
G	1.0	1.00	5778	1.73e-2
K	0.8	0.84	4500	8.75e-3
M	0.5	0.57	3500	3.64e-3

list of sources. Although included in FastChem 3, we have not made use of the condensation due to the fact that the temperatures at all pressure of our models are above 1900 K - which is greater than the point of condensation for all the included gas species (Kitzmann et al. 2024). If this work were to be repeated for colder planets or non-inverted atmospheres, then condensation would likely start to play a major role.

3.2.3 Star-planet systems

For all of the models, we assume that the planet is $\simeq 1.5$ R_{earth}. We tested four star-planet systems, each with a star of a different spectral type (F, G, K, and M). For each system, we placed the planet at an orbital distance from the star that corresponds to the distance at which the equilibrium temperature at the substellar point is equal to 3000 K. This was determined using:

$$d_{\rm orb} = R_{\rm star} \left(\frac{T_{\rm eq}}{T_{\rm star}} \right)^{0.5} \tag{3.2}$$

Where R_{star} and T_{star} are the radius and temperature of the host star and T_{eq} is the desired equilibrium temperature. For the G type star, we chose to use the equilibrium temperature and mass of the sun, while for the other three, we used representative temperatures and masses of each spectral type. We used a standard mass-radius relationship of $R_{star} \propto M^{0.8}$ (Kippenhahn et al. 2012) to determine the radius of the stars. An overview of the system parameters we used for each spectral type is given in Table 3.1.

Stellar types hotter than F type star ($T_{star} > 7300$ K) are not included in this work. This is due to the apparent rarity of HREs orbiting such stars, with only two detections to date (Charpinet et al. 2011; Morton et al. 2016), and the planet to star flux ratio that is obtained from these systems[4] is too low to

[4] About 2 ppm at 1 μm and 30 ppm at 20 μm for a 1.5 R_{earth} planet at an orbital distance

be able to observe accurately with current generation telescopes.

3.2.4 Radiative transfer

In order to calculate the TP profiles of the tested atmospheres (step **3**), we used the radiative-transfer code HELIOS (Malik et al. 2017, 2019; Whittaker et al. 2022). As in Zilinskas et al. (2023), these TP profiles were self-consistently calculated with the output of FastChem and LavAtmos, such that the final surface temperature is consistent with the overall atmospheric chemistry. As explained in step **4** at the start of the methods section, this is achieved by iterating until the surface temperature used to calculate the vapour composition is the same as the temperature at the bottom of the TP-profile.

In all cases, we used the standard diatomic adiabatic coefficient $\kappa = 2/7$ for convective adjustment. For our opacities, we used all of the atomic and molecular species that are included in our melt compositions. This includes atoms Al, Ca, Fe, K, Mg, Na, Si, Ti, as well as molecular species AlO, CaO, MgO, O_2, SiO, SiO_2, and TiO[5]. The line lists were kept the same as in (Zilinskas et al. 2023), with atomic species using the Vienna Atomic Line Database (VALD3) (Ryabchikova et al. 2015) and the molecular species from a range of sources. All of the line lists that we used and their corresponding sources can be found in Table 3.3. Note that these opacities were sourced from the DACE[6] database or calculated using HELIOS-K (Grimm & Heng 2015; Grimm et al. 2021). In Figure 3.13, we show the unweighted opacities of some of the most important atmospheric species.

We used the `PHOENIX` models (Husser et al. 2013) to calculate the stellar spectra for each of the F, G and K spectral types. Just as in Zilinskas et al. (2023), we combined the `PHOENIX` spectrum for an M type star with scaled shortwave `MUSCLES` spectra (France et al. 2016; Loyd et al. 2016; Youngblood et al. 2016) so as to accurately model the increased shortwave emission seen in cooler stars. See Figure 3.14 for a side by side comparison of the included stellar spectra.

For step **6**, we pass the output of the chemistry and temperature structure to `petitRADTRANS`[7] (Mollière et al. 2019, 2020), which we use to compute the final emission spectrum. Where possible, the opacity line lists were kept the same as in `HELIOS`, but the opacities themselves were obtained from ExoMol[8] pre-packaged correlated-k tables (Chubb et al. 2021). All of the spectra were calculated using the low-resolution mode of $\lambda/\Delta\lambda = 1000$, with a wavelength range of 0.3 – 28 µm.

of 4.44e-2 AU (equivalent to a substellar equilibrium temperature of 3000K) for a BSE vapour only atmosphere.

[5]Although FeO is abundant in lava-vapour atmosphere, there are currently no available line lists for this molecule and is therefore not included in the radiative transfer model.

[6]https://dace.unige.ch/

[7]Version 2.7.6

[8]https://www.exomol.com/

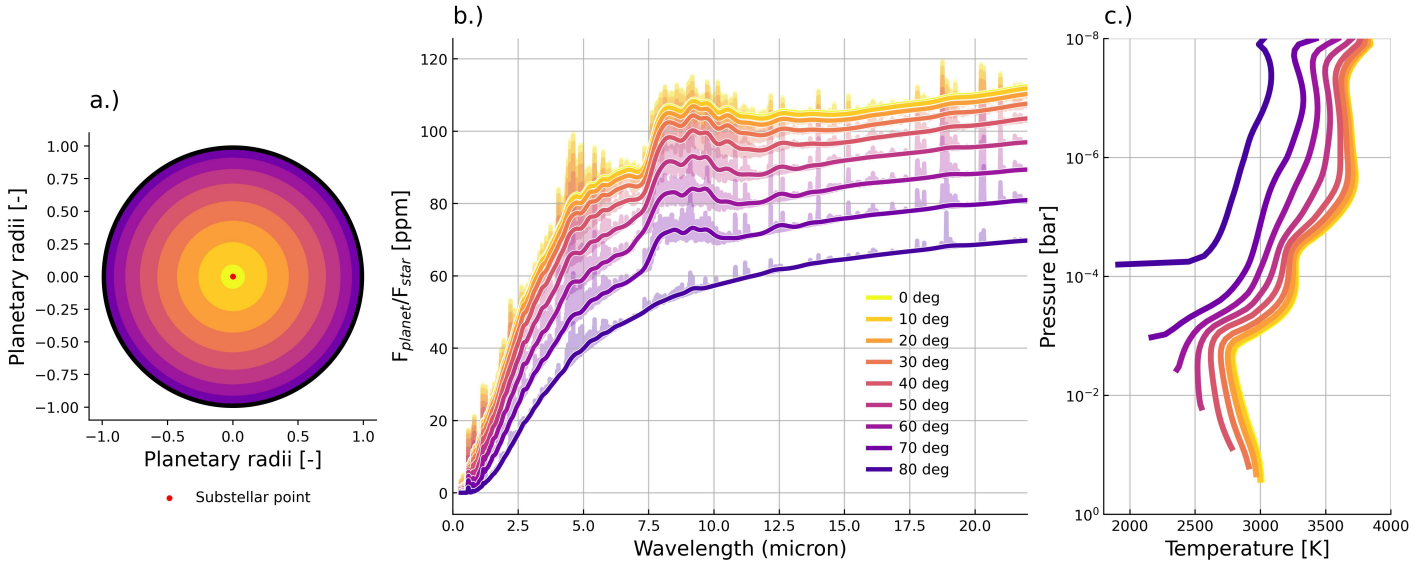

Figure 3.2: Pseudo-2D atmosphere model: Panel a.) shows the area from which light is emitted from different angles of separation from the substellar point (shown using a red dot). In panel b.) we show the different spectra that are calculated for each of the different rings. Panel c.) shows the TP profiles for each ring, illustrating how the surface temperature (the bottom of the profile) decreases with increasing distance from the substellar point.

3.2.5 Pseudo-2D model

In order to alleviate some of the drawbacks of modelling thermal emission from a 3D object using a 1D approach, as previously done in Zilinskas et al. (2022, 2023), we expanded our method to a pseudo-2D approach. This was first used in Zieba et al. (2022) to model the atmosphere of the planet K2-141 b and has since then also been used to rule out a melt vapour-only atmosphere for 55-Cnc e in Hu et al. (2024).

In Figure 3.2, we illustrate how this approach works in detail. We calculate the 1D emission spectrum at 10° intervals moving away from the substellar point (panel *a* in Figure 3.2). Moving away from the sub-stellar point increases the zenith angle, leading to less stellar irradiation hitting the surface of the planet, hence, lowering the surface temperature. This is demonstrated in panel *c*. The spectra calculated at each angle are then weighted according to the surface area covered by each interval and summed, giving a single averaged spectrum of the entire day-side of the planet. This approach allows us to take into account how melt vapour composition changes as a function of surface temperature and the effect that this has on the spectral features in the emission spectrum.

In Figure 3.15, we show a comparison between this approach (shown in light blue) and another commonly used approach of using a day-side averaged temperature estimation (shown in orange). The comparison was made using a bulk silicate earth (BSE) composition (Palme & O'Neill 2003) around a G type star. In this comparison, we can see that the pseudo-2D approach leads to slightly less pronounced features and a slight increase in the continuum spectrum, most notably at wavelengths beyond 5 μm (panel *b*).

3.3 Results

As explained in section 3.2, we produced models for F, G, K, and M type stars, varying the melt oxide abundances of SiO_2, MgO, Al_2O_3, TiO_2, FeO, CaO, Na_2O, and K_2O. We found that the melt species that had the strongest influence on the temperature-pressure profile and emission spectrum of a generic HRE with a substellar temperature of 3000 K are TiO_2 and SiO_2. This is covered in detail in the following subsections of this paper along with some tentative indications that Na and K could also play a potentially observable role in HRE emission spectra and TP profiles. For the remaining species, however, varying their abundance in the melt oxides did not lead to any significant effects on the shape of the emission spectra and TP profiles and are therefore not shown in the results.

Before delving into the results, we first devote a subsection to analysing in detail the temperature-pressure and chemical structure as well as the opacity contributions and the resulting emission spectrum of a BSE atmosphere for a G-type star with an equilibrium temperature of 3000 K. This will help explain and interpret the results in the following sections.

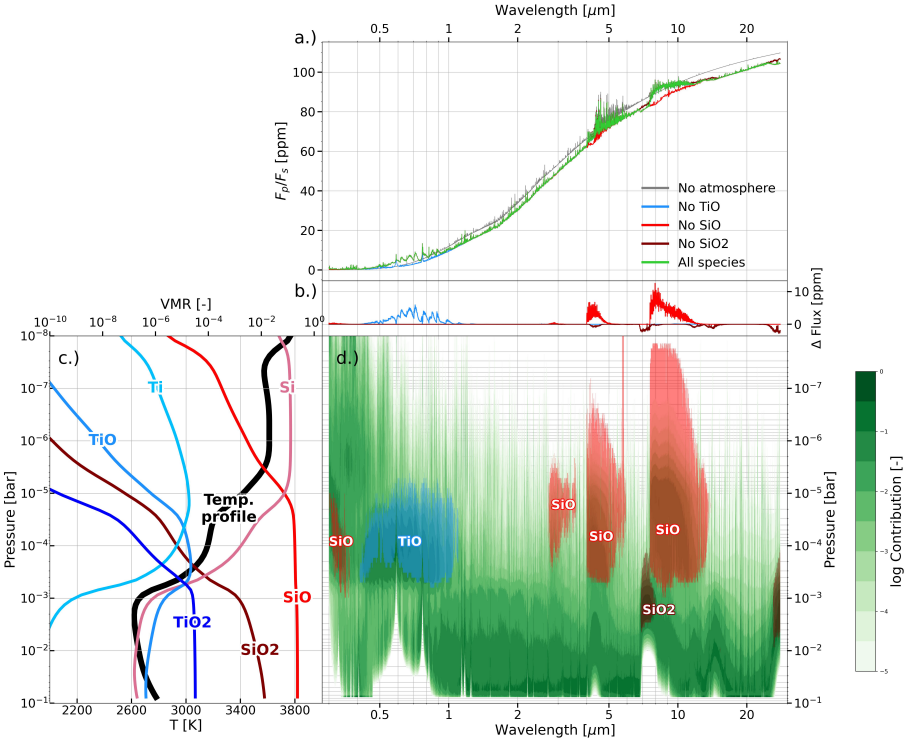

Figure 3.3: Overview of a vapour atmosphere: Each of these panels represent different aspects of a vaporised atmosphere above a BSE melt for a G-type star at 40° from the substellar point. In the top panel (a) we compare the emission spectrum when including all species (green) with cases where a single specified opacity is excluded. The panel below that,(b), shows the difference in ppm between the spectrum containing all species and the ones with the opacity of one species removed. The bottom left panel (c), contains both the temperature-pressure profile of the atmosphere (in black) as well as the VMR of a few keys species in the atmosphere. Finally, in the bottom right panel (d)) the contribution to the emission as function of pressure and wavelength is visualised. We highlighted the regions where the contribution from key species is most prominent.

3.3.1 The anatomy of a BSE vapour atmosphere

To understand how a changing melt and atmosphere composition affects the emission spectrum of an HRE, it is useful to first visualise where the emission originates in the atmosphere. In Figure 3.3, we show the chemistry, the emission spectrum, and the contribution function of a rock vapour atmosphere above a melt with a BSE composition. For this model, we assumed the same parameters as that of a planet orbiting a G-type star (see Table 3.1). We assume incident irradiation equivalent to that at 40° away from the substellar point due to this resulting in similar temperatures as the averaged temperature of a pseudo-2D model (see Section 3.2.5).

In the top panel (*a*) of Figure 3.3, we show the calculated emission spectrum for the case with no atmosphere (grey), an atmosphere containing the full list of species (green, see Table 3.3 for details on each species), and three spectra calculated with a single species omitted - TiO, SiO, and SiO_2 (blue, red, and maroon respectively). In order to highlight the changes in flux when removing these species from the opacities, we added a panel below (*b*) in which we plot the difference in ppm between the spectra. It should be noted that for the spectra with the omitted species, we only left out the opacity of these species when calculating the emission spectrum using petitRADTRANS (step **6** in Section 3.2), so the temperature-pressure profile was calculated assuming the presence of all species and remains the same. The leftmost panel (*c*) contains both the temperature-pressure structure of the atmosphere (in black, x-axis located at the bottom), as well as the volume mixing ratios (VMR) of a selection of atmospheric species (coloured, x-axis located at the top). The panel to the bottom right (*d*) shows the opacity contribution as a function of wavelength and pressure. Regions with especially strong contributions from SiO, SiO_2, and TiO are highlighted (red, maroon, and blue respectively).

Looking at the spectrum for the case with no atmosphere in panel *a*, we see that including an atmosphere leads to an overall decrease in flux. This is due to the major emitting region (also known as the photosphere) in the model containing an atmosphere being located in a region of the atmosphere (between 1e-1 and 1e-2 bar) which has a lower temperature than the surface. Similarly, the SiO_2 features around 7 μm show up as absorption features in the spectrum due to originating from a relatively colder part of the atmosphere - coinciding with 1e-3 bar, the lowest temperature region of the atmosphere.

As we go beyond this point to higher altitudes and lower pressures around 1e-4 bar, TiO and SiO become the spectrally dominant species. As explained in Gandhi & Madhusudhan (2019), thermal inversions occur in atmospheres where

$$\kappa_{\rm vis}/\kappa_{\rm ir} \gtrsim 1 \tag{3.3}$$

Where κ_{vis} is the average opacity in the optical wavelength range (between about 0.1 and 1 μm) and κ_{ir} the average opacity in the infrared (beyond $\simeq$ 3μm). Looking at the contribution plot (panel *d*), we see a strong increase in

the opacity in the optical, which, despite the SiO opacity contribution in the infrared, is enough to satisfy the criterion in equation 3.3, leading to a thermal inversion. The presence of a thermal inversion allows for emission features in the spectrum (Gandhi & Madhusudhan 2019), which we see clearly for TiO around 0.7 μm and for SiO at 3, 4.5, and 8 micron. Going up further into the atmosphere, the opacity contribution of these species decreases, coinciding with the decrease in their abundance at lower pressures, as can be seen by comparing panel *c* to panel *d*. The more complex species disassociate into their atomic counterparts with increasing temperature and decreasing pressure.

Thanks to the strong influence on both the thermal structure of the atmosphere and the emission spectrum of SiO, SiO_2, and TiO, we find that varying the abundance of SiO_2 and TiO_2 in the melt has a significant effect on the emission spectra of HREs. This is covered in detail in the following subsections. Besides the aforementioned species, there are a few other species that may have an observable effect on the emission spectrum of HREs (Zilinskas et al. 2022). However, we find that only Na and K could potentially lead to some observable changes if their corresponding melt end-member species (Na_2O and K_2O) are changed. This is explored in the final subsection of the results.

3.3.2 TiO_2 variation

In Figure 3.4, we show how varying the TiO_2 melt abundance affects the VRM of TiO throughout the atmosphere for a planet orbiting a G-type star[9]. The change in VMR of TiO at a given pressure is almost in linear relation to the change in abundance of TiO_2 in the melt. However, we do see a decrease in surface pressure as a result of decreasing surface temperature. In Figure 3.5 we show in detail how a varying TiO_2 melt abundance affects the emission spectrum (panels in the left column), and the temperature pressure profile (panels in the right column) for F, G, K, and M type stars. The temperature profiles shown are those calculated at a 40° angle away from the sub-stellar point as they were deemed most representative of the average dayside (see Figure 3.2). To allow for a clearer visualization of the differences in the spectra, we added a panel below panels containing the emission spectra showing the difference in flux between the spectra calculated using the BSE (indicated with the '1 x TiO_2' label) composition and those with varying levels of TiO_2.

The behaviour of the emission spectra and TP profiles is qualitatively similar for planets orbiting F-, G-, and K- type stars, which we will describe first, after which we will focus on the results of planets orbiting an M- type star. Changing the TiO_2 melt abundance - and as a result the TiO atmospheric abundance - of these planets has a significant effect on both the temperature-pressure profile of the atmosphere and its emission spectrum. The two most notable effects are 1) a significant decrease in the surface temperature and 2) an

[9]The relative behaviour of TiO shown in Figure 3.4 is representative for the behaviour of F-, K- and M- type stars as well.

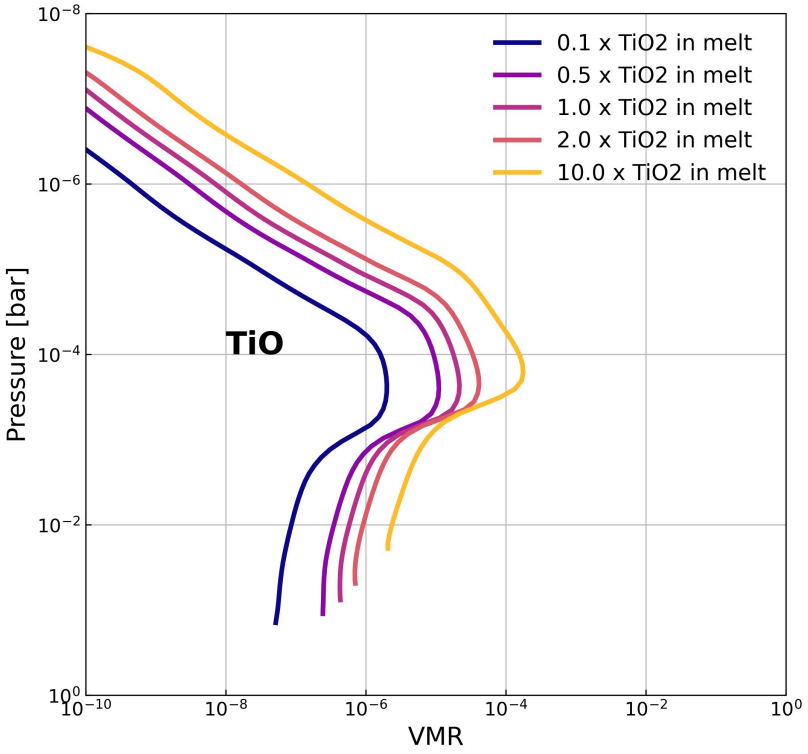

Figure 3.4: Atmospheric TiO changing with TiO_2 melt abundance: Shown for a planet orbiting a G-type star (see Table 3.1 for parameters). The TiO_2 abundance in the melt was changed with respect to the BSE abundance (see Table 3.2).

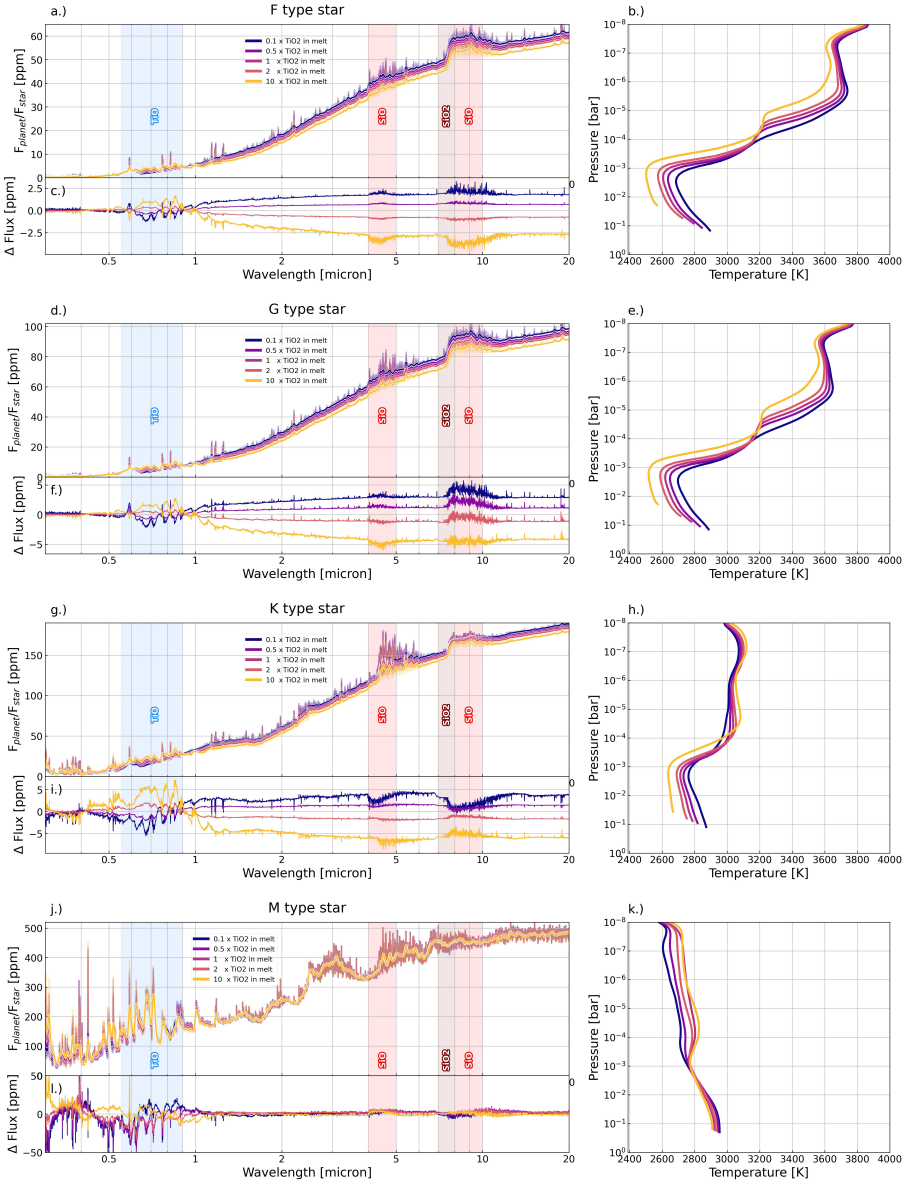

Figure 3.5: Effect of varying TiO_2 melt percentage on emission spectra - For an F-, G-, K-, and M-type star we show the calculated pseudo-2D emission spectra and TP profiles for different TiO_2 melt abundances. Under each spectrum we also plot the differences in flux between the different spectra with respect to 1 x TiO_2 melt (which is the same as a BSE composition). The TP profiles shown are those for the models calculated at a 40° angle away from the substellar point. Note the difference in the scales of the y-axes of the emission spectra for the different stellar types.

increase in the size of the TiO emission features (highlighted in blue in Figure 3.5).

The decrease in surface temperature, from around 2900 K to 2550 K for the F- and G-type stars and from 2850 to 2650 K for K-type stars, is due to the increase in TiO abundance leading to an increase in the opacity of the atmosphere in the optical wavelengths (see panel *d* in Figure 3.3). This allows less of the stars irradiation to reach the planet's surface, decreasing its temperature, leading to a significantly lower flux being emitted from the planet, as is shown in panels *c*, *f*, and *i*, where we see a decrease in flux of up to 5 ppm in the infrared (with respect to the BSE case) for a 10x increase in TiO_2 abundance.

In the upper atmosphere, however, the temperatures converge again up around 3900 K. Hence, as the TiO_2 melt abundance (and the TiO atmospheric abundance) increases, the size of the temperature inversion increases as well. Looking back at equation 3.3, we see that this is what one would expect for an increase in the opacity in the optical wavelength range. The result of the strengthening of the temperature inversion and increasing TiO atmospheric abundance with increasing TiO_2 melt abundance, is that even with an overall decrease in flux, the TiO emission features grow.

Comparing the low TiO_2 abundance TP profiles with their high abundance counterparts for F- and G- type stars also shows that in atmospheres with abundant TiO_2 the TP profile becomes almost isothermal between 1e-4 and 1e-5 bar - which coincides with the pressures with the highest TiO abundance (see Figure 3.4) and also the pressures from which the greatest opacity contribution in the optical is located (see Figure 3.5).

All of the changes to the emission spectrum and temperature pressure profile caused by varying the TiO_2 abundance, are due to the changing absorption of irradiation within the optical. Hence, the spectra of planets orbiting F- and G-type stars, which emit the majority of their energy in the optical wavelengths (see Figure 3.14), are affected more than for cooler K-type stars. This is most visible in the temperature pressure profiles in Figure 3.5. Those calculated for K-type stars have far weaker thermal inversions and are close to isothermal above 1e-4 bar. This trend of decreasing thermal inversion strength was also found for hot-Jupiters by Lothringer & Barman (2019) and was also shown for HREs in Zilinskas et al. (2022). What should be noted though, is that the planet to star flux ratio is higher for cooler/smaller stars, hence the differences in the size of the TiO_2 emission features are greater than that of hotter stars, reaching up to 5 ppm, despite the smaller temperature inversion.

Looking at the spectrum of a planet orbiting an M-type star in the bottom row of Figure 3.5, we see that varying TiO_2 melt abundance does not seem to have a very significant effect on the emission spectrum or TP profile of the planet. This is due to the fact that the emission peak of M-type stars is shifted so far to the red (see Figure 3.14) that the high opacity of TiO in the optical does not block as significant an amount of the radiation as for the hotter stars.

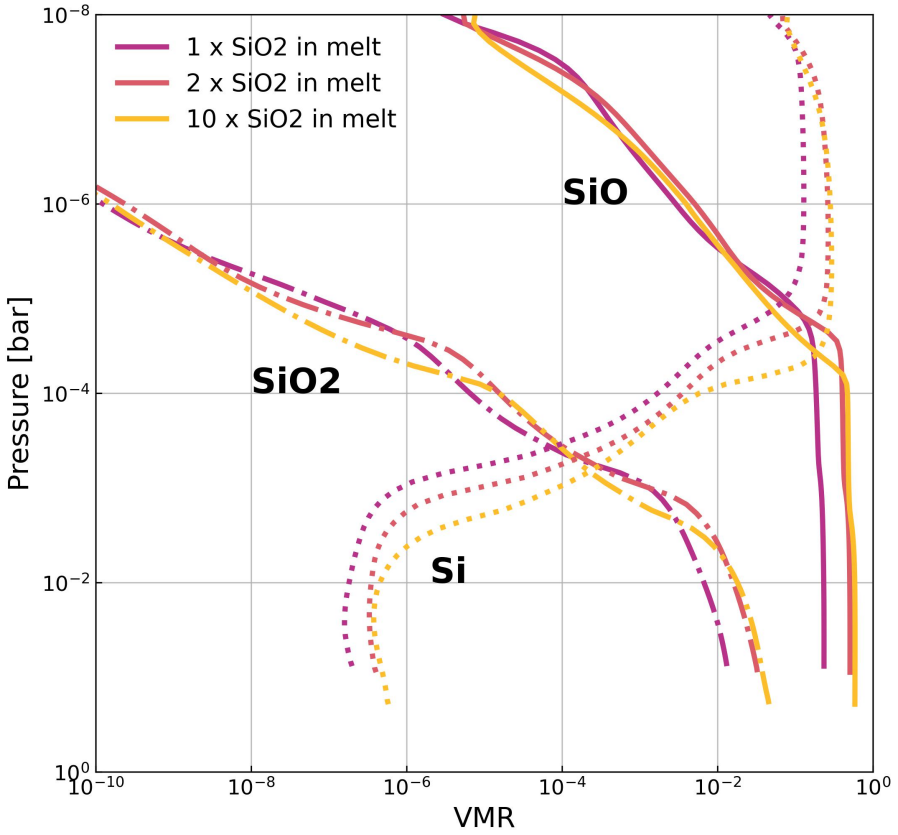

Figure 3.6: Atmospheric SiO and SiO_2 changing with SiO_2 melt abundance: Shown for a planet orbiting a G-type star (see Table 3.1 for parameters). The SiO_2 abundance in the melt was changed with respect to the BSE abundance (see Table 3.2).

Hence, the surface temperature is not affected as strongly and the overall flux level remains about the same for all TiO_2 melt abundances. Furthermore, the relatively small temperature inversion and generally lower temperature of the atmosphere leads to far less prominent emission features, making it more difficult to discern the planetary atmosphere features from the features in the stellar spectrum.

3.3.3 SiO_2 variation

As mentioned in section 3.2, we were not able to model a decrease in SiO_2 abundance in the melt composition due to `MELTS` not being able to run for compositions with low SiO_2 abundance. In Figure 3.6 we show the VMR of the

most important Si species in the atmosphere of a G-type star at 40° degrees away from the substellar point. In contrast to varying TiO_2 melt abundance and its effect on TiO atmospheric abundance, increasing SiO_2 melt abundance does not lead to an increase of SiO or SiO_2 throughout the entire atmosphere. Lower in the atmosphere (at higher pressures) an increase in SiO_2 melt abundance does lead to an increase in SiO and SiO_2 atmospheric abundance. However, as we can see in panel *e* (the TP profile of the planet orbiting a G-type star) in Figure 3.7, the changing melt composition affects the TP profile such that there is an increase in temperature with increasing SiO_2 beyond 1e-2 bar. This temperature increase is enough to cause SiO and SiO_2 to start dissociating into Si lower in the atmosphere. This causes the SiO and SiO_2 VMRs to be about equal for all melt abundances at pressures below 1e-3 and 1e-5 bar respectively. SiO and SiO_2 have the greatest amount of opacity contributions at greater pressures, so the spectra of these atmospheres still see significant changes.

Increasing SiO_2 melt abundance leads to an increase in surface temperature for the planets around all four tested stellar spectral types. The temperature increase is caused by a relative decrease in TiO_2 in the melt as SiO_2 melt abundance is increased. SiO_2 makes up such a large fraction of the total melt composition ($\simeq$ 45% in BSE), that changing its abundance also significantly affects the abundances of the other melt species. The resulting decrease in TiO_2 abundance leads to an increase in temperature similar to that seen in the previous section where we decreased TiO_2 melt abundance directly.

Increasing the abundance of SiO_2 in the melt causes the temperature inversion to take place at higher atmospheric pressures. This is due to a combination of: 1) higher surface temperatures, 2) an increase in IR opacity due to more abundant atmospheric SiO_2 and SiO, and 3) a decrease in the optical opacity with less abundant atmospheric TiO. For the planets orbiting the F-, G-, and K-type, this moves the thermal inversion from around 1e-3 bar to around 1e-2 bar for a 10x increase in SiO_2.

This change moves the temperature inversion from a region in the atmosphere above the SiO_2 opacity contribution to a region below it (see Figure 3.3), turning the SiO_2 absorption feature between 7 and 8 μm into an emission feature. This indicates that detecting an SiO_2 emission or absorption feature in the emission of an HRE could constrain the pressure/altitude at which a thermal inversion takes place.

Although the temperature inversion starts at a higher pressure and with a higher minimum temperature, the increase in IR absorption leads to the higher temperatures higher up in the atmosphere (as mentioned above as well). This causes the overall size of the temperature inversion to remain the same, but shifted towards higher temperatures for greater SiO_2 melt abundances. This, in combination with a greater abundance of SiO in the atmosphere, leads to very prominent SiO emission features (at 4.5 and 9 mum) at high SiO_2 melt abundance which are up to 10 ppm greater for G-type stars and around 7

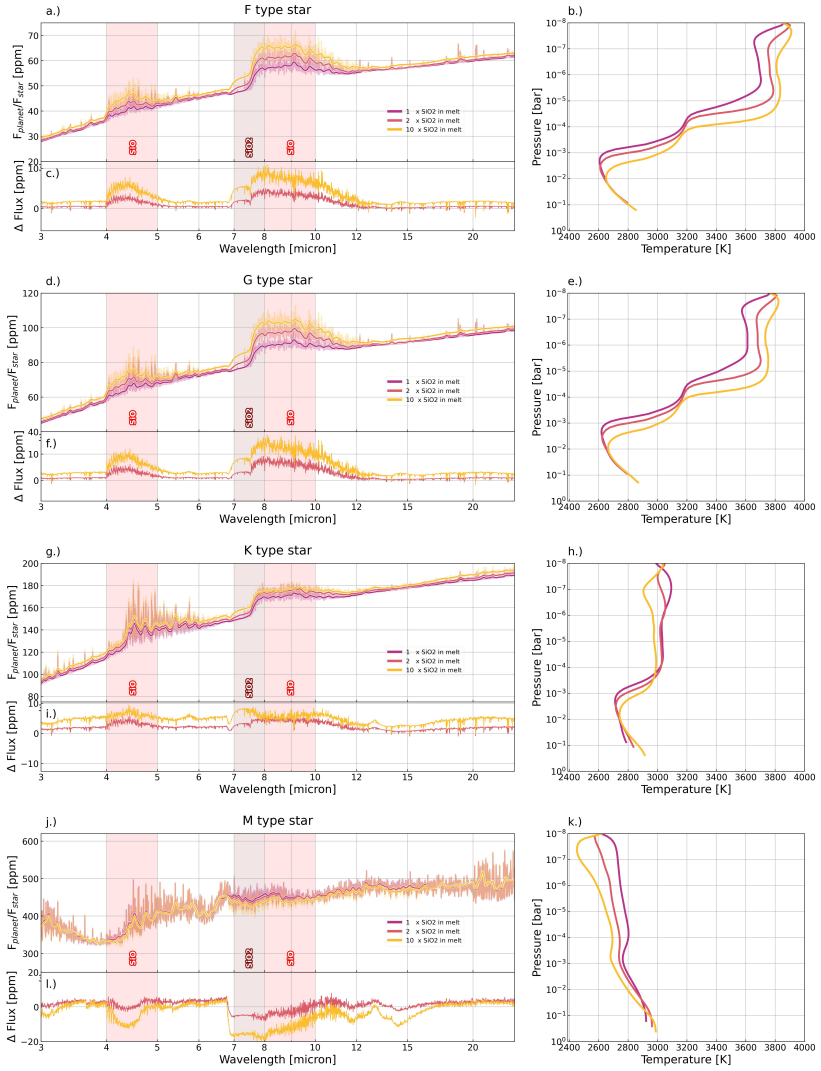

Figure 3.7: Effect of varying SiO_2 melt percentage on emission spectra - For an F-, G-, K-, and M-type star we show the calculated pseudo-2D emission spectra and TP profiles for different SiO_2 melt abundances. Under each spectrum we also plot the differences in flux between the different spectra with respect to 1 x SiO_2 melt (which is the same as a BSE composition). The TP profiles shown are those for the models calculated at a 40° angle away from the substellar point. Note the difference in the scales of the y-axes of the emission spectra for the different stellar types.

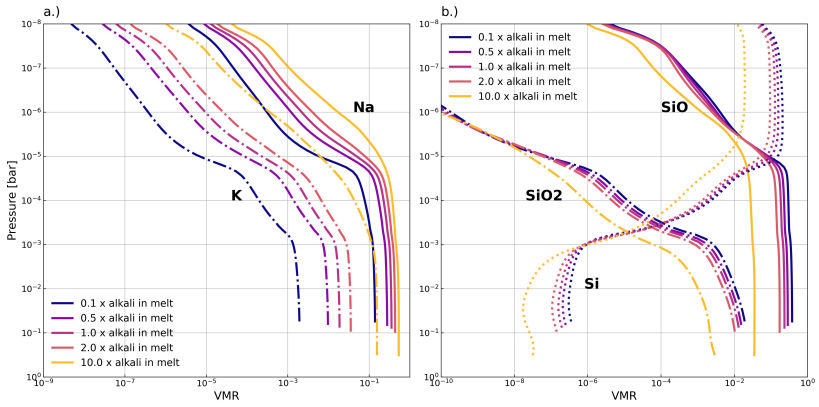

Figure 3.8: Atmospheric species changing with alkali melt abundances: Shown for a planet orbiting a G-type star (see Table 3.1 for parameters). The alkali oxide (Na_2O and K_2O) abundances in the melt were changed with respect to the BSE abundance (see Table 3.2).

ppm greater for F and K type stars than that of the BSE composition spectra (Figure 3.7).

For planets orbiting M-type stars (bottom row in Figure 3.7) we see different behaviour than for the hotter spectral types. Just as what we saw for TiO_2 melt abundance variation, increasing SiO_2 melt abundance decreases the temperature inversion strength down to the point where it is almost non-existent and most of the atmosphere is non-inverted. This leads to the atmospheric SiO and SiO_2 features becoming absorption features instead of emission features. Although difficult to discern when overlaying the spectra over each other, it becomes clearer when we look at the flux difference between the BSE case and the increased SiO_2 melt abundance models.

3.3.4 Alkali variation

Atmospheric Na and K do not contribute as significantly over broad wavelengths to the opacity of the atmosphere as TiO, SiO, and SiO_2. Hence, they do not have as strong an influence on the TP profile or low-resolution spectrum of HRE exoplanet atmospheres. However, as can be seen in Figure 3.13, they do have a number of lines across the optical and the near-infrared. They are also some of the most volatile species released in melt vaporisation from Na_2O and K_2O (Fegley & Cameron 1987; Schaefer & Fegley Jr. 2004; Zilinskas et al. 2022; van Buchem et al. 2023; Wolf et al. 2023). As such, varying the abundance of Na_2O and K_2O in the melt has a strong effect on the atmospheric abundances of Na and K. We decided to vary Na_2O and K_2O abundance concurrently due to the similarity of their behaviour.

In Figure 3.8 we show the VMR of atmospheric Na and K (in panel *a*) for

different variations of the alkali oxide (Na_2O and K_2O) abundances in the melt at an angle of 40° away from the substellar point for a G-type star. Decreasing the alkali abundance by an order of magnitude relative to the BSE abundance (0.1x) leads to a drop in total surface pressure from 7.63e-2 bar to 5.52e-2 bar, while increasing the alkali abundance by an order of magnitude increases the total surface pressure to 3.21e-1 bar. Looking at Figure 3.9 - we see that this is not due to a change in surface temperature (as we saw for TiO_2 and SiO_2) but due to an increase in vaporised Na and K. Although Figure 3.8 focuses on a planet orbiting a G-type star, we see a similar increase in surface pressure for all host star spectral types, as can be seen in the TP profiles shown in Figure 3.9. This could be of consequence to models that take heat and material redistribution over the day/night side of the planet into account (e.g. Nguyen et al. 2024).

Increasing the melt abundance of Na_2O and K_2O and the resulting increase in Na and K in the atmosphere leads to broadening of their features in the optical. The strongest effect is seen for the K features between 0.75 and 0.8 μm (see Figure 3.9). There are also a number of emission lines between 1 and 3.5 μm from atmospheric K that see significant growth of (up to 10 ppm for planets orbiting a K-type star) with increasing alkali melt abundance - these are indicated in light blue in Figure 3.9. Although the Na feature at 0.6 μm appears to broaden slightly, its peak decreases in height. This is likely due to our model not being of high enough spectral resolution to fully visualize this feature. Further work in high resolution is required to draw any definite conclusions.

Varying the abundance of alkali species in the melt significantly affects the SiO and SiO_2 atmospheric abundance, as shown in panel *b* of Figure 3.8. As a result, the SiO and SiO_2 features in the emission spectrum vary (see Figure 3.9) and the temperature structure of the atmosphere is affected (most significantly above 1e-5 bar). This effect on the atmospheric Si species is partly due to the change in abundance of SiO_2 in the melt after renormalization (similar to the change in TiO_2 abundance when increasing SiO_2 abundance in the previous subsection). However, this change in abundance is relatively small due to the alkalis making up but a small percentage of the total melt composition. Besides melt abundance, the activity (see section 3.2.2) of a species in a melt is also determined by the activity coefficient (γ). In an ideal case, this is equal to one but due to the complex nature of melts this value is usually less than one. As shown in Hirschmann et al. (1998), increasing the alkali contents of a melt decreases the activity coefficient of SiO_2 due to reducing the number of Si-O-Si linkages. In Figure 3.16 we plot both the activity of SiO_2 and its weight percentage in the melt, illustrating this effect.

We do not see any significant changes in the spectrum of the M-type star and hence do not include it. All of the models that we ran for this work can be found on GITHUB OR ZOTERO LINK.

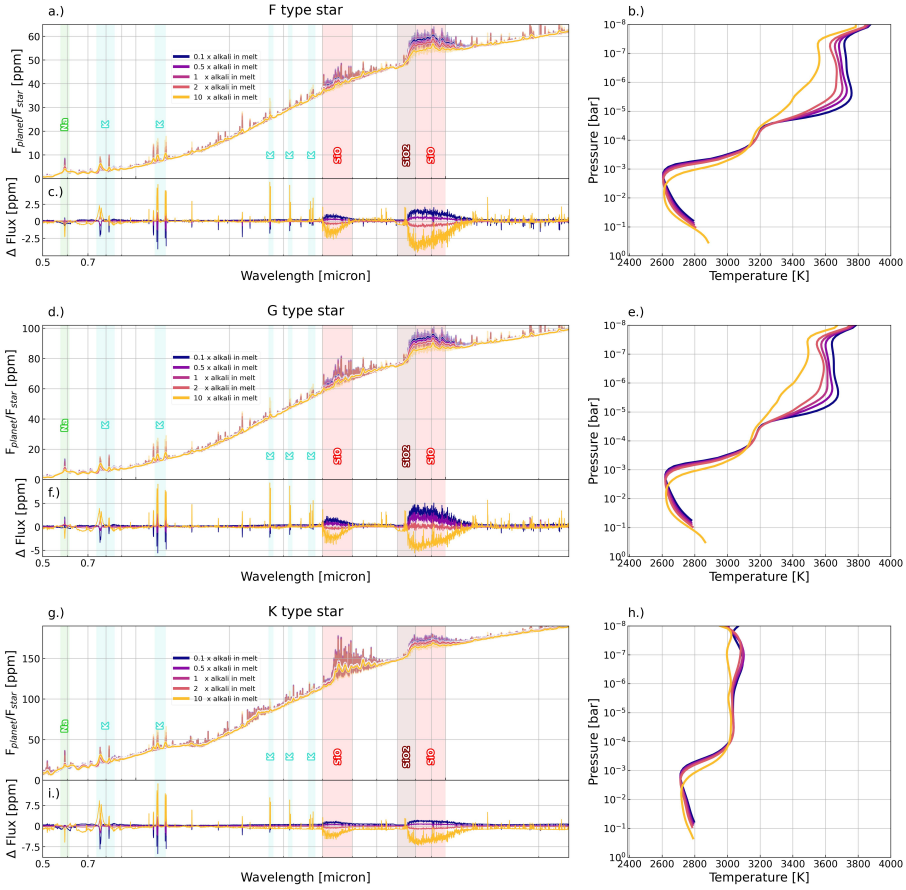

Figure 3.9: Effect of varying Na_2O and K_2O melt percentage on emission spectra: For an F-, G-, and K-type stars, we show the calculated pseudo-2D emission spectra and TP profiles for different SiO_2 melt abundances. Under each spectrum we also plot the differences in flux between the different spectra with respect to 1 x alkali abundances (which is the same as the Na_2O and K_2O weight percentages in a BSE composition). The TP profiles shown are those for the models calculated at a 40° angle away from the substellar point. Note the difference in scales of the y-axes of the emission spectra for the different stellar types.

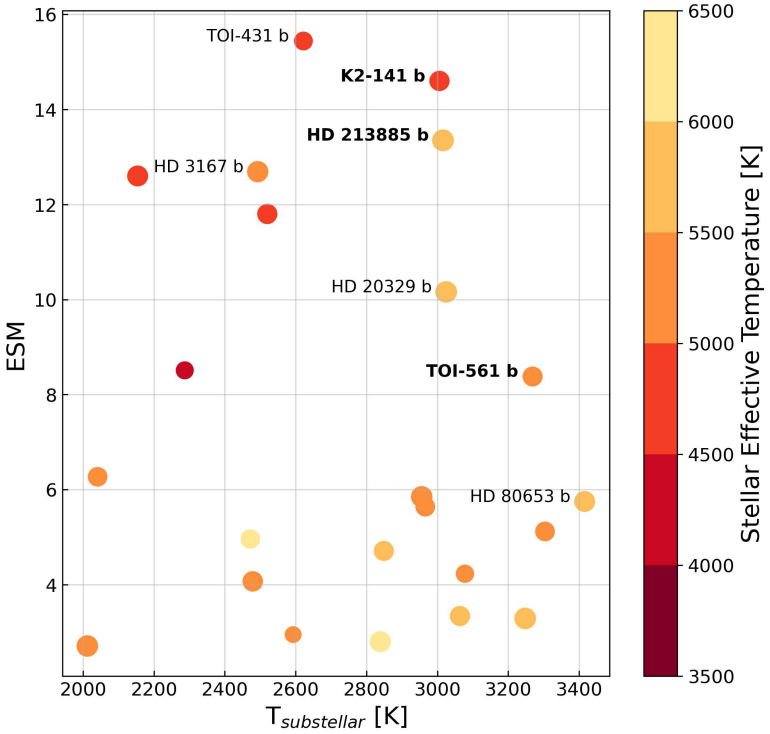

Figure 3.10: Potential observing targets - A selection of confirmed exoplanets with a radius of $< 2R_{\oplus}$ and with a substellar equilibrium temperature > 2000 K. On the y-axis we plot the emission spectroscopy metric (ESM) as defined in Kempton et al. (2018). The planets labelled in bold are those we selected for error bar estimates shown in Figures 3.12 and 3.11.

3.3.5 Observability of potential targets

With the aim of estimating the feasibility of observing variations in the HRE spectra due to changes in melt composition using JWST, we simulated eclipse observations for three different HREs. We then derived the expected precision in measuring their emission spectra for a number of different JWST instruments. In Figure 3.10, we plot a selection of confirmed HREs with a radius $< 2R_{\oplus}$ and with a substellar equilibrium temperature > 2000 K. We plotted them as a function of substellar temperature on the x-axis and their emission spectroscopy metric (ESM) on the y-axis. The ESM, as defined in Kempton et al. (2018), is a useful indicator of the expected S/N of a JWST secondary eclipse observation at mid-IR wavelengths. We also coloured the planets according to the effective temperature of their host stars. We selected HD 213885 b, TOI-561 b, and K2-141 b due to their high ESM values and substellar equilibrium temperatures, as well as covering a range of different stellar spectral types for their host stars. For our simulated observations we used the open source code `PANDEXO` (Batalha et al. 2017) and assumed six eclipses. We chose a number of groups per integration that is $\leq 80\%$ of full well-depth in order to avoid reaching saturation. We assumed an optimistic noise floor of zero ppm.

In Figures 3.11 and 3.12, we show the estimated error bars alongside TiO_2 and SiO_2 variation respectively. For HD 213885 b, we used the system parameter values published in Espinoza et al. (2020). Due to the brightness of the star HD 213885 ($V_{mag} = 7.95$, $J_{mag} = 6.81$), the number of instruments that can be used to observe it without over-saturating is limited, inhibiting observations below 2.5 μm. However, for the instruments with which can observe, the error bars are relatively small, at around 5 ppm at best for NIRSpec G395H. This could potentially allow for the extreme cases of 0.1x and 10x TiO_2 to be discerned from each other. Due to the difference in flux coming from a change in surface temperature and not a distinct feature, this would have to be complemented with some optical data (covering 0.5-1 μm) indicating the presence of TiO in the atmosphere. For SiO_2 abundance variation (Figure 3.12) we see that the error bars for NIRSpec G395H may be small enough to allow one to discern a BSE melt composition from a melt with a 10x SiO_2 abundance increase based on the 4-5 μm feature. Similarly, MIRI LRS may have enough sensitivity to discern these two aforementioned models at the SiO_2 and SiO features between 7 and 10 μm.

For TOI-561 b and K2-141 b, we used the system parameters published in Brinkman et al. (2022) and Zieba et al. (2022) respectively. Although it is possible to use greater number of instruments to observe TOI-561 b and K2-141 b without over-saturation, most error bars are too large to be able to discern any of the models with certainty. For TiO_2 variation (Figure 3.11), NIRSpec G140H and G235H may be able to discern 0.1x and 10x TiO_2 abundance from each other. However, just as with HD 213885 b, the difference in flux is coming from a decrease in surface temperature leading to a lower continuum emission and not from a specific spectral feature. Hence, without the detection of the TiO

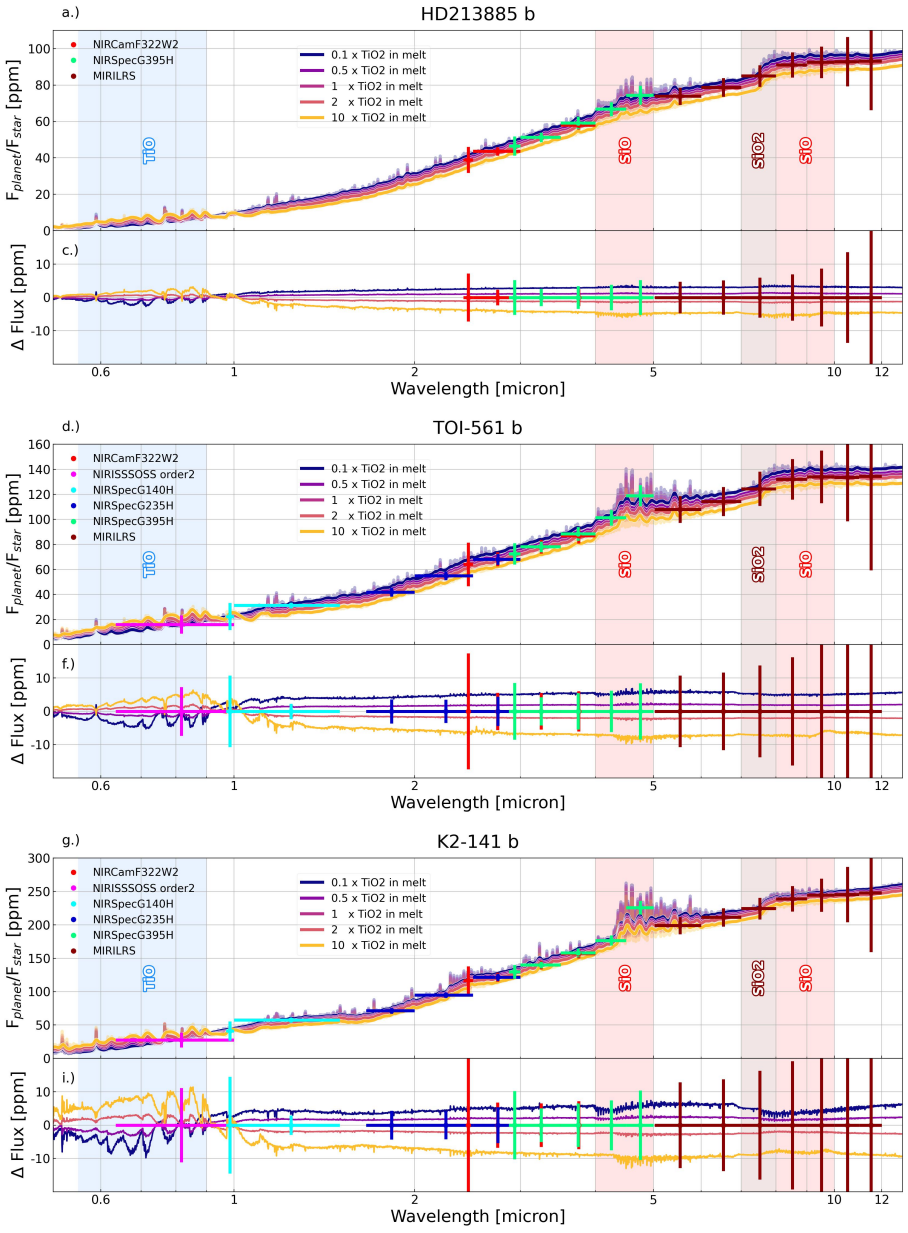

Figure 3.11: JWST error bar estimates for TiO_2 variation - Error estimates were calculated using `PANDEXO` (Batalha et al. 2017) for 6 eclipses.

feature at 0.5-1 μm, it would be difficult to know if the change in temperature is due to the presence of TiO in the atmosphere or due more efficient heat-redistribution than expected. NIRISS SOSS could potentially have been used to break this degeneracy, but does not appear to be sensitive enough. For SiO_2 variation neither NIRSpec G395H nor MIRI LRS appear to be sensitive enough to convincingly discern the different melt compositions from each other.

Overall, it appears difficult to discern changes in melt compositions of HREs using only JWST spectroscopy. The most promising target seems to be HD 213885 b, for which, as of the writing of the paper, there are no planned JWST observations. Observations would likely be most useful if combined with (potentially) Earth-based optical high-resolution spectra that could be used to discern specific species in the atmosphere.

3.4 Discussion

3.4.1 Melt compositions

In section 3.2.1, we have shown (Figure 3.1) that the tested compositional ranges cover the compositional variation of bulk silicate reservoirs derived from stellar compositions (Putirka & Rarick 2019). However, studies of the early chemical evolution of rocky bodies in our own solar system show that the possible range in composition of lava oceans is likely to be significantly larger. The evolution of Earth's Moon serves as a good example. A wide range of geochemical evidence suggests that the Moon was fully molten shortly after its formation in the aftermath of a giant impact on Earth (e.g. Steenstra et al. 2020). At this time the lunar core segregated from the lunar mantle, and the composition of the molten surface was equal to the composition of the whole silicate reservoir. Subsequently, the Moon formed a $>$ 30km thick primary crust formed primarily by the mineral plagioclase (e.g. Elkins-Tanton et al. 2011; Lin et al. 2017), with a composition far richer in Al, Ca, and Si, and far poorer in Fe, Mg, and Ti, than this initial bulk silicate reservoir. Subsequent volcanism concentrated on the lunar nearside then led to the formation of a range of lavas rich in Mg, and Fe, exhibiting a range in TiO_2 concentrations up to $>$15 wt. per cent, well beyond the maximum of the range of lava compositions based on bulk silicate abundance estimates (Figure 3.1). All other rocky bodies in the inner solar system show crustal compositions that are both different from bulk silicate compositions and that vary across the surface. Clearly geological processes can significantly expand both absolute and relative element abundances of surface materials.

3.4.2 Assumptions made in our model

The model used for this work is a pseudo-2D model that assumes thermochemical equilibrium (see section 3.2). This does not take into account chemical

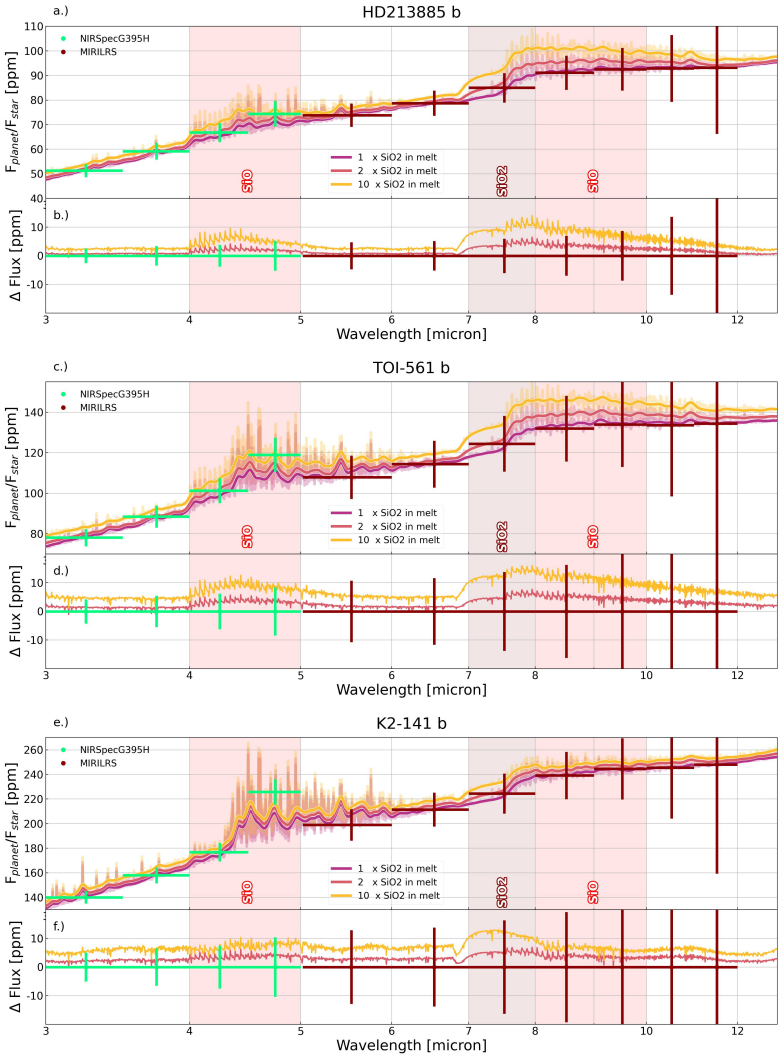

Figure 3.12: JWST error bar estimates for SiO_2 variation - Error estimates were calculated using `PANDEXO` (Batalha et al. 2017) for 6 eclipses.

kinetics that may be taking place higher up in the atmosphere where strong UV radiation could lead to chemical dissociation. Due to the high temperatures of the modelled atmospheres, it is likely that a chemical equilibrium approach provides a good approximation of the atmospheric chemistry. In order to investigate whether photochemistry could have a significant influence, chemical pathways for silicates are needed, which are currently unavailable in literature.

We do not take condensation into account either. As shown in Nguyen et al. (2024), this could have some effect on the temperature structure of the planet at different longitudes. Future work could be focused on combining condensation calculations with a pseudo-2D model to take the resulting changes in temperature structure and (potentially) cloud opacity into account.

The fact that we focus on low resolution spectra means that our results do not rule out that other melt oxide species could be important to high resolution spectral analysis.

3.4.3 Surface temperature degeneracy

As discussed in the results section and as shown in Figures 3.5 and 3.11, varying TiO_2 melt abundance, directly influences TiO atmospheric abundance, which has a very strong influence on the surface temperature of the planet. This is due to its strong optical opacity.

Concluding that an HRE atmosphere contains TiO because the apparent surface temperature is lower than what one would expect without TiO, would be ignoring other key factors that can affect planetary surface temperatures and should therefore not be used as direct evidence. For example, in Hu et al. (2024), the emission spectrum found for 55-Cnc e pointed to a surface temperature of several hundreds of Kelvin lower than expected for a bare lava-vapour atmosphere. This was attributed to the presence of a volatile (potentially carbon-rich) atmosphere leading to more efficient heat-redistribution from the day- to the night-side. Other studies have shown that the presence of clouds may have a significant effect on surface temperatures as well (Nguyen et al. 2024; Loftus et al. 2024).

Conversely, future interpretations of HRE emission spectra should also consider the effect that a significant TiO abundance in the atmosphere could have on the temperature-pressure structure of a lava planet. A potential way to disentangle the resulting degeneracy would be to try and observe the TiO emission feature found between 0.55 and 0.9 μm.

3.5 Conclusion

We investigated how varying the abundances of oxide melt species at the surface of a lava planet affects its atmospheric emission spectrum. We modelled the atmospheres and resulting emission spectra using chemically self-consistent pseudo-2D models for dry HREs orbiting F-, G-, K-, and M-type host stars.

We find that the melt species which have the most significant influence on the emission spectra of HREs are TiO_2 and SiO_2.

TiO_2 melt abundance dictates atmospheric TiO abundance, which, due to its strong optical opacity, heavily influences the surface temperature of the planet if it orbits an F-, G-, or K- type star. This change in surface temperature affects both the total pressure of the vaporised atmosphere and its composition - affecting the strength of emission features of species such as SiO. The decrease in temperature caused by the presence of TiO affects all but the upper reaches of the atmosphere, leading to a drop in the continuum of emission of the planet. A potential way to discern this drop in temperature as being due to the presence of TiO and not due to efficient heat-redistribution is by observing the TiO optical emission feature.

Increasing the SiO_2 melt abundance leads to a significant increase in the strength of the atmospheric SiO and SiO_2 features in the infrared for planets orbiting F-, G-, and K-type stars. It also leads to stronger and deeper temperature inversions, below the point where SiO_2 has the highest opacity contribution. This leads to the SiO_2 feature flipping from being an absorption feature to being an emission feature.

Varying the melt abundance of the alkali oxides Na_2O and K_2O influences the abundance of atmospheric Na and K respectively. This affects the K (and single Na) spectral features in the optical and near-infrared, which may merit further investigation with high-resolution modelling for HRE planets orbiting F-, G-, or M-type stars. The increase in atmospheric Na and K at relatively large melt abundances of Na_2O and K_2O lead to a large increase in the total pressure of the atmosphere. This could potentially be of importance for heat-redistribution models.

Varying the alkali abundance in the melt also affects the activity of the SiO_2 in the melt, with greater alkali abundances leading to lower SiO_2 activities. This significantly impacts the abundances of atmospheric Si species and hence the strength of the SiO and SiO_2 features in the emission spectrum.

To estimate the observability of these changes in emission spectra due to changes in melt composition, simulated JWST observations for HD213885 b, TOI-561 b, and K2-141 b. These planets were selected due to their high infrared observability metric (ESM) and high surface temperatures. We found that with six eclipses, only the most extreme differences in melt composition may be discernible from each other in the infrared for HD213885 b, and in the near-infrared for TOI-561 b, and K2-141 b.

Acknowledgements

This work was supported financially through a Dutch Research Council (NWO) Planetary and Exoplanetary Science (PEPSci) grant awarded to Y.M. and W. van W. Y.M and M.Z. acknowledge funding from the European Research Council (ERC) under the European Union's Horizon 2020 research and innovation

programme (grant agreement no. 101088557, N-GINE). R. B. acknowledges funding from the Oort and Legaat Kruytbosch Scholarship.

Data Availability

The data underlying this article is available upon reasonable request from the author.

Appendix

3.A Melt compositions

The melt compositions are calculated by multiplying their original BSE weight percentage, as given in Palme & O'Neill (2003), by different factors (0.1, 0.5, 2, and 10). This leads to weight percentages of greater than 100 for some species. This is not an issue for LavAtmos due to the fact that the composition is normalized internally. However, it may give a wrong impression of the actual abundance that is being tested. Hence, we provide a table below showing the varied weight percentages for each of the species for which we present results (indicated with *Before norm.*) as well as their normalized counterparts (indicated with *After norm.*). Note that SiO_2 abundances lower than BSE could not be tested due to limitations of the MELTS code.

Table 3.2: Melt composition variation

	Multiplier								
	x0.10		**x0.50**		**x1**	**x2**		**x10**	
Species	Before norm. [%]	After norm. [%]	Before norm. [%]	After norm. [%]	**BSE**	Before norm. [%]	After norm. [%]	Before norm. [%]	After norm. [%]
SiO_2	-	-	-	-	**4.54E+01**	9.08E+01	6.24E+01	4.54E+02	8.93E+01
TiO_2	2.10E-02	2.10E-02	1.05E-01	1.05E-01	**2.10E-01**	4.20E-01	4.19E-01	2.10E+00	2.06E+00
Na_2O	3.49E-02	3.50E-02	1.75E-01	1.75E-01	**3.49E-01**	6.98E-01	6.96E-01	3.49E+00	3.38E+00
K_2O	3.10E-03	3.10E-03	1.55E-02	1.55E-02	**3.10E-02**	6.20E-02	6.20E-02	3.10E-01	3.09E-01

Table 3.3: Opacity data: List of opacities and their sources used to calculate the temperature-pressure profiles and emission spectra in this work. Those with DACE as indicated source were taken directly from the DACE database (`https://dace.unige.ch/`). For the other species, the opacities were calculated using HELIOS-K (`https://github.com/exoclime/HELIOS-K`) (Grimm & Heng 2015; Grimm et al. 2021).

Species	Source	Line list	Line list reference
Al	DACE	VALD	Ryabchikova et al. (2015)
AlO	HELIOS-K	ATP	Patrascu et al. (2015)
Ca	DACE	VALD	Ryabchikova et al. (2015)
CaO	HELIOS-K	VBATHY	Yurchenko et al. (2016)
Fe	DACE	VALD	Ryabchikova et al. (2015)
K	DACE	VALD	Ryabchikova et al. (2015)
Mg	DACE	Kurucz	Kurucz (1992)
MgO	HELIOS-K	LiTY	Li et al. (2019)
Na	DACE	VALD	Ryabchikova et al. (2015)
Si	DACE	VALD	Ryabchikova et al. (2015)
SiO	HELIOS-K	SiOUVenIR	Yurchenko et al. (2022)
SiO_2	DACE	OYT3	Owens et al. (2020)
Ti	DACE	VALD	Ryabchikova et al. (2015)
TiO	HELIOS-K	Toto	McKemmish et al. (2019)
Scattering and continuum			
O_2	Scattering		Gray (2008)
O_2-O_2	petitRADTRANS		Mollière et al. (2019, 2020)

3.B Opacity data

3.C Stellar spectra

3.D Pseudo-2D atmosphere

3.E SiO_2 activity changing with alkali abundances

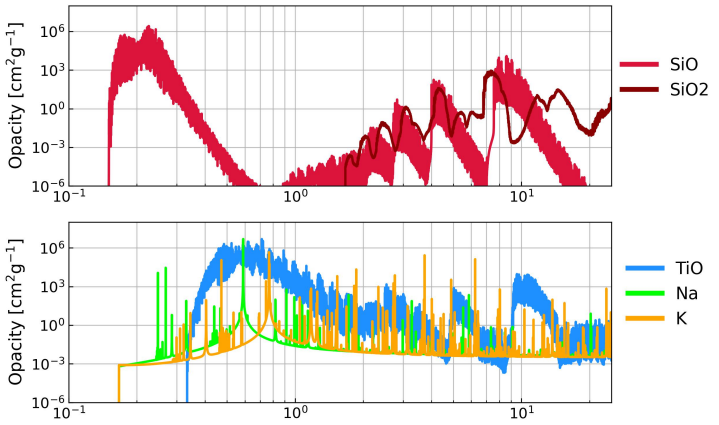

Figure 3.13: Opacities of important atmospheric species: The unweighed opacities of SiO, SiO_2, TiO, Na, and K are shown here for a temperature of 2700 K and 1e-2 bar. See Table 3.3 for the line lists used to calculate the opacities shown here.

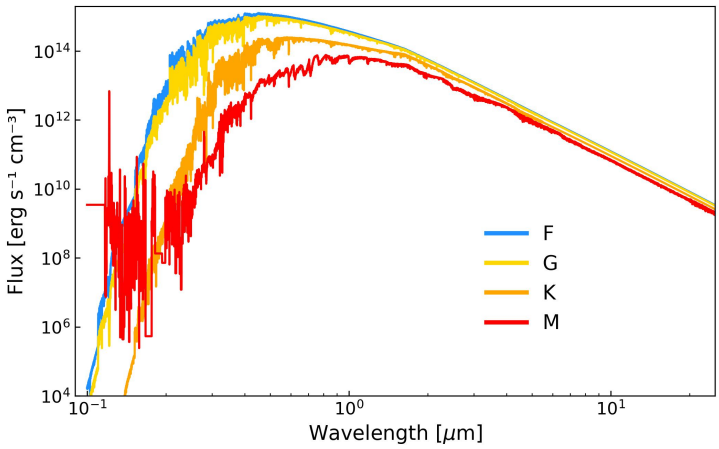

Figure 3.14: Stellar spectra used for each of stellar type: The spectra for the F, G, and K stars were calculated using the `PHOENIX` models. For the M type star we combined the `PHOENIX` model with scaled `MUSCLES` shortwave spectra.

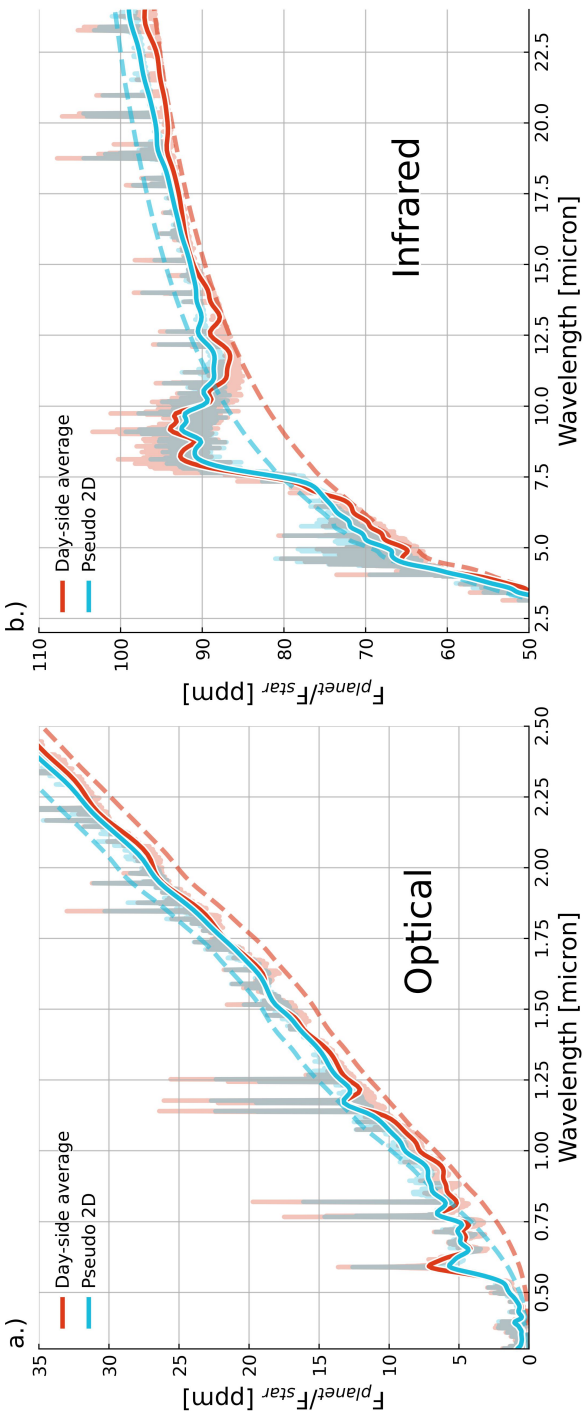

Figure 3.15: Comparison between a pseudo-2D model and a dayside averaged model: The low resolution day-side averaged spectrum is shown in orange, the pseudo-2D approach is shown in light blue. The higher resolution version of the spectra or shown using a lower opacity in the background and the spectra for an empty atmosphere (airless rock) on the same planet is shown using the dashed lines. The left panel (a) shows the spectra within the optical wavelength range, while the right side panel (b) shows the spectra within the infrared wavelength range.

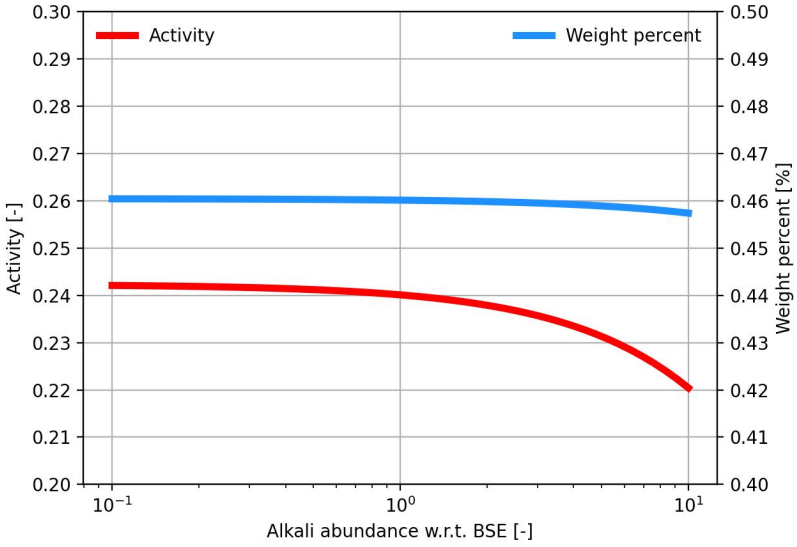

Figure 3.16: SiO_2 melt activity as a function of changing alkali abundances: Calculated using ThermoEngine, the python wrapper to MELTS (Ghiorso & Sack 1995).